Geocarto International

ISSN: 1010-6049 (Print) 1752-0762 (Online) Journal homepage: https://www.tandfonline.com/loi/tgei20

Markov random field-based method for super-resolution mapping of forest encroachment from remotely sensed ASTER image

L.K. Tiwari, S.K. Sinha, S. Saran, V.A. Tolpekin & P.L.N. Raju

To cite this article: L.K. Tiwari, S.K. Sinha, S. Saran, V.A. Tolpekin & P.L.N. Raju (2016) Markov random field-based method for super-resolution mapping of forest encroachment from remotely sensed ASTER image, Geocarto International, 31:4, 428-445, DOI: 10.1080/10106049.2015.1054441

To link to this article: https://doi.org/10.1080/10106049.2015.1054441

Geocarto International, 2016
Vol. 31, No. 4, 428–445, http://dx.doi.org/10.1080/10106049.2015.1054441

Taylor & Francis
Taylor & Francis Group

Markov random field-based method for super-resolution mapping of forest encroachment from remotely sensed ASTER image

L.K. Tiwari[a]*, S.K. Sinha[a], S. Saran[c], V.A. Tolpekin[b] and P.L.N. Raju[c]

[a]*Department of Earth Science, Rajiv Gandhi Institute of Petroleum Technology, Rae Bareli, India;* [b]*Faculty of Geo-Information Science and Earth Observation, Department of Earth Observation Science, University of Twente, Enschede, The Netherlands;* [c]*Department of Space, Indian Space Research Organization, Indian Institute of Remote Sensing, Dehradun, India*

(*Received 30 December 2014; accepted 19 May 2015*)

Forest encroachment (FE) is a problem in Andaman and Nicobar Islands (ANI) in India for environment and planning. Small gaps created in the forest slowly expand its periphery disturbing the biodiversity. Therefore, intrusion of poachers, slash and burn and other factors causing FE must be carefully detected and monitored. Remote sensing offers a great opportunity to accomplish this task because of its synoptic view. Conventional classification methods with remotely sensed images are problematic because of small size of FE and mixed landcover composition. This study presents an application of super-resolution mapping (SRM) based on Markov random field for detection of FE using ASTER (15 m) images. The SRM results were validated using multispectral IRS LISS-IV (5.8 m) image. Non-contiguous FE patches of various sizes and shapes are characterized using the spatial contextual information. The novelty of this approach lies in the identification and separability of small FE pockets which could not be achieved with pixel-based maximum likelihood classifier (MLC). The SRM parameters were optimized and found comparable to previous studies. Classification accuracy obtained with SRM at scale factor 3 is $\kappa = 0.62$ that is superior to accuracy of MLC ($\kappa = 0.51$). SRM is a promising tool for detection and monitoring of FE at Rutland Island in ANI, India.

Keywords: forest encroachment; super-resolution mapping; maximum likelihood classifier; Markov random field

1. Introduction

Small encroachments inside a forest land, such as illegal felling of trees, shifting cultivation, cleared patches in woodlands and their detection on remotely sensed images are challenged by the resolution of different satellite sensors and limited contrast with the background or surrounding landcover. Several studies have been conducted to detect and map such small landscape elements (SLE) using high-resolution data such as aerial photographs, IKONOS images and coarse resolution images such as SPOT-4 multispectral images (Dijkstra et al. 2003; Groom et al. 2006; Oosterbaan & Pels 2007; Sheeren et al. 2009; Skaloš & Engstová 2010). However, high-resolution remotely sensed images have large spectral variations for the same classes and local variation within the homogeneous fields (Tolpekin & Stein 2009). Also, high-resolution satellite images have fewer spectral bands than coarse resolution sensors for landcover classifications

*Corresponding author. Email: lktiwari@rgipt.ac.in

(Vega et al. 2006; Tolpekin & Stein 2009). Several studies have used super-resolution mapping (SRM) techniques on coarse resolution image to enhance its spatial resolution and at the same time to benefit from its available higher spectral bands for landcover classification (Tatem et al. 2001, 2002; Kasetkasem et al. 2005; Boucher & Kyriakidis 2006; Boucher 2009). In our case, ASTER image has 15 m of spatial resolution and we have performed super-resolution technique based on Markov random field (MRF) with scale factor of 3.

1.1. Studies on FE

Remotely sensed images taken at different times with different sensors have been used in identification of forest encroachment (FE) (Sastry et al. 2007; Mehdawi & Bin Ahmad 2012; Grinand et al. 2013; Kumar et al. 2013; Satish et al. 2014). On-screen visual image interpretation technique with time series change analysis has been used to assess forest cover change on a grid of 1 km in Nilgiri Biosphere Reserve, Western Ghats, India (Satish et al. 2014). On the Eastern part of the United States and in the central Brazil area, detection of forest cover change from 1960s to 2000s was carried out on Corona and Landsat images using support vector machine (SVM) and textural analysis (Song et al. 2014). Textures within window size of 7 × 7 pixels, 9 × 9 pixels and 11 × 11 pixels provided most informative matrices for forest classification in remotely sensed images of Corona. In a hybrid approach where remote sensing images of IRS LISS-III sensor and GIS technique was combined with visual interpretation method to study FE in Belgaum Dist, Karnataka, India, (Kumar et al. 2013) and for the entire state of Manipur, India (Sastry et al. 2007). Among the often used image enhancement techniques like Look up table stretch, histogram equalization, histogram match, haze reduction, Sastry et al. (2007) reported that histogram equalization worked better for FE mapping. FE study in Mabira forest reserve, Uganda, was carried out by systematic sampling technique and survey/interview (Baranga 2007). Optical and microwave image fusion technique followed by sub-pixel and object-oriented classification methods were used to detect and monitor illegal logging and tropical rain FE in east Kalimantan, Indonesia (Vega et al. 2006). They also reported that the principal component analysis-based fusion technique was best suited to detect shifting cultivation and sub-pixel classification could detect single tree felling inside the forest land. Stone et al. (1991) estimated deforestation using supervised, unsupervised classification techniques, visual interpretation and GIS on Landsat and AVHRR satellite data.

In this study, encroached area or FE is considered as the combination of more than one landcover class including scattered forest/planted trees, agricultural crops, waterbody and a group of huts. Till date, there is no standard or globally accepted definition of FE or defined by international organization such as Food and Agriculture Organization or United Nations Organization. Commission on Agriculture, Government of India in 1976, had defined FE as an unauthorized of forest produce and diversion of such forest land to non-forest land use/cover practices including jhumming in which FE is considered as a part of forest degradation.

1.2. Studies on MRF-based mapping

In an unsupervised change detection technique, Subudhi et al. (2014) used fuzzy Gibbs Markov random field (GMRF) to get difference image of the multi-temporal and multispectral remotely sensed data. Ghosh et al. (2013) combined GMRF with Hopfield

neural network for unsupervised change detection classification of multi-temporal images. In both the studies of unsupervised change detection, the problem is solved through the maximum a posteriori (MAP) estimation principle. An algorithm for fusion of multispectral remotely sensed images, based on MRF wherein they have incorporated contextual information into fusion model for better interpretation, is provided by Xu et al. (2011). Bruzzone and Prieto (2000) automated the MRF technique for unsupervised change detection analysis based on image differencing from multi-temporal remotely sensed satellite data. Ardila et al. (2011) and Tolpekin et al. (2010) performed SRM based on MRF technique, assessed their potential and validated them using ground survey, VHSR and digital aerial photographs. They also performed object-oriented and pixel-based accuracy assessment of their outputs. SRM was conducted on normally distributed synthetic images in Tolpekin and Stein (2009). Ardila et al. (2011) used VHSR images for detection of tree crowns in urban areas of the Netherlands using MRF-based SRM with contextual and probabilistic information. The results from this classification method outperformed in comparison with the maximum likelihood and SVM-based results. It is very crucial to determine the goal of SRM in terms of its dimension (binary or multivariate) and resolution (low or high resolution or somewhere between the two) (Atkinson 2009). Various algorithms for SRM can essentially be divided into two categories. One is regression-type or learning algorithms which include geostatistical model building, linear mixer models and feed-forward back propagation type artificial neural networks (ANN). Spatial optimization algorithms, such as pixel swapping, simulated annealing and Hopfield neural network fall into the second category. Tolpekin and Stein (2009) introduced smoothness parameter to control the balance between probabilistic and contextual information in the posterior energy function for class separation on SRMs. Optimal smoothness parameter produces more accurate estimates of class area proportion compared to those obtained with linear spectral unmixing used in sub-pixel/soft classification. Kasetkasem et al. (2005) reported that MRF-based SRM enhances the landcover classification.

1.3. Motivation for MRF-based SRM

There are several techniques of SRM, such as sub-pixel mapping based on genetic algorithm (Mertens et al. 2003), pixel swapping technique with mathematical morphology (Mertens et al. 2006), Hopfield neural network (Tatem et al. 2001, 2002), MRF with simulated annealing (Kasetkasem et al. 2005) and others. For soft classification in SRMs wherein the reliability of class area proportion is limited in the individual pixels of the remotely sensed coarse resolution images, Tatem et al. (2002) used Hopfield neural network, while Mertens et al. (2003) used genetic algorithm. However, MRF integrates spectral with contextual information (Kasetkasem et al. 2005; Tolpekin & Stein 2009). MRF-based SRM takes into account spatial distribution of class proportions within pixels (Atkinson 1997). According to Li (2009), MRF models accurately map the spatial dependence between the classes and their proportions within and in the neighbouring pixels. MRF models have been used to redefine the results from a sub-pixel classification. An MRF model does not depend upon the availability of an accurate sub-pixel classification (Tolpekin & Stein 2009). In this study, we have successfully implemented MRF-based contextual SRM method as described in Tolpekin and Stein (2009), on remotely sensed ASTER images in identifying FE. In this approach, smoothness parameter is estimated beforehand based on local energy balance

analysis on training sets. Four classes have been generated and they are as follows: encroached area, waterbody, forest and degraded forest/land.

2. Study area

Our study area is located in the north-western part of the Rutland Island, Andaman and Nicobar Islands (ANI), India, (Figure 1) between latitude 11°28′00″N to 11°20′00″N and longitude 92°35′00″E to 92°45′00″E. The area lies in the South Andaman district of the Union Territory of ANI. Rutland Island (approx. 14,028 ha in area) bears a unique stunted formation of southern hilltop forest dominated by Dipterocarpuscstatus (with an average height below 10 m). Highest peak in Rutland is Mount Ford – 435 m above mean sea level. FE will be studied in this Study area.

3. Method

The method used for FE identification is essentially an SRM technique based on MRF method. We have used ASTER image as a test bed and LISS-IV image for validation purpose. An SRM technique, often used in landcover classification, produces a thematic map with finer spatial resolution than that of the given multispectral remotely sensed image. Here qualitative and quantitative accuracy assessment of SRM is compared with the output of maximum likelihood classification (MLC).

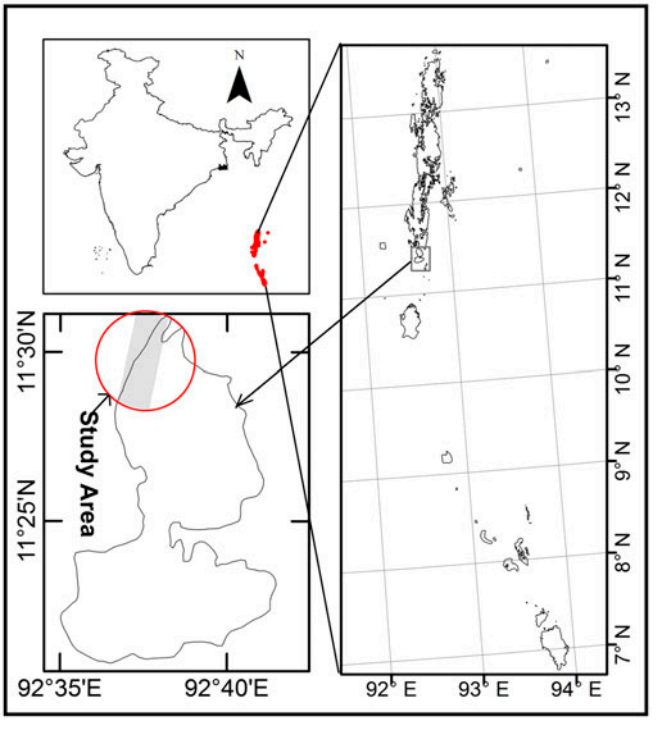

Figure 1. The shaded area in the circle shows study area in the north-western part of Rutland Island, which is a part of archipelago in Indian Ocean, Andaman and Nicobar Islands.

3.1. Proposed scheme of the study

In this study, Level 1b ASTER image is to be processed for SRM with MRF method to map FEs. Scale factor of 3 was decided for the desired resolution of 5 m from the ASTER image of 15 m resolution. Proposed scheme of the study is shown in Figure 2. Other available data from Google Earth and LISS-IV is reprojected in the UTM projection system similar to ASTER image. To prepare class statistics from ASTER image, LISS-IV and Google Earth data are used. Reference map is digitized from LISS-IV data with visual aid from Google data of 60 cm resolution. MLC map is generated with these class statistics and downscaled MLC map becomes the initial map for SRM processing. Parameterization of MRF method follows simulated annealing algorithm. Optimized SRM map as output is then compared with MLC map; statistical accuracy assessment is performed and verified with the field data.

3.2. Super-resolution mapping

Atkinson (1997) introduced SRM, which is essentially a sub-pixel mapping, to identify spatial dependence within and between the pixels using three different approaches, ANN, mixer modelling and fuzzy logic. They obtained the most appropriate result with neural network. A comprehensive introduction to SRM is given in Atkinson (2004) and Tatem et al. (2001). Spatial dependence of sub-pixels leads to an increase in resolution of SRMs (Thornton et al. 2006).

We adopted degradation model (Equation (1)) as described in Tolpekin and Stein (2009). Let y be a multispectral remote sensing image containing K spectral bands with spatial resolution R, which is coarse resolution. The pixel locations are denoted as $b_i \in B$, where B is the pixel matrix with size $M \times N$. We assume existence of

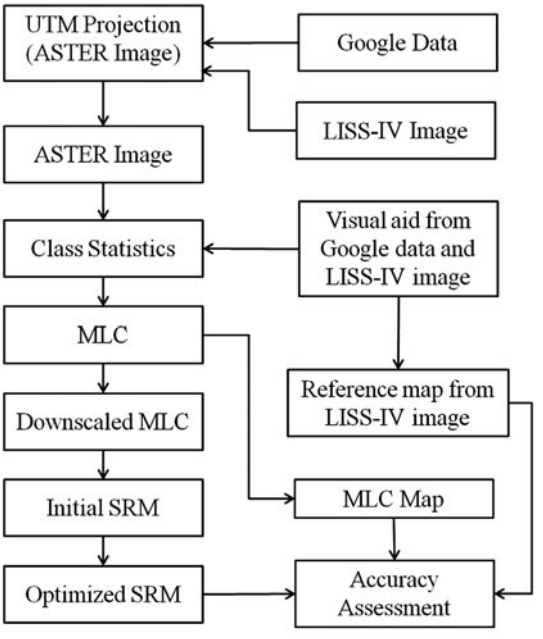

Figure 2. Flow diagram showing proposed scheme of the study.

multispectral image (x) defined on a set of pixels A with finer spatial resolution, r, having K spectral bands. The pixel set A covers the same area on the earth surface as B. Scale factor S is an additional input parameter in SRM wherein we get landcover maps of various spatial resolutions for a given input image. The scale factor $S = \frac{R}{r}$ is assumed to be an integer. Finer resolution pixels $a_{j|i}$, where $j = 1, \ldots S^2$ form A of matrix size $(\mathrm{SM}) \times (\mathrm{SN})$. The super-resolution map is represented by c, which has finer resolution with the same spectral resolution. Here x is our assumed image and c is the estimated super-resolution map. Downscaled MLC of multispectral image y is used as an input to obtain an initial estimate of c. Furthermore, a unique class (α) is assigned to each pixel in the image x, such that $c(a_{j|i}) = \alpha$, where $\alpha \in \{1, 2. \ldots \ldots L\}$. The degradation model for the images y and x is established as:

$$y(b_i) = \frac{1}{S^2} \sum_{j=1}^{s^2} x(a_{j|i}) \tag{1}$$

Now, with each pixel ($a_{j|i}$) located at the centre of a window size W, symmetric neighbourhood $N(a_{j|i})$ is introduced on A, which is a set of pixels inside the square window obtained from image x. Li (2009) describes the neighbouring relationship properties in detail. First-order and second-order neighbourhood are the most popular ones, which correspond to four and eight closest pixels, respectively.

3.3. *Markov random fields*

MRF is a mathematical tool which is used to incorporate prior and likelihood information to yield good classification results of the input remotely sensed images. MRF takes into account priori wherein it considers contextual information between the neighbouring pixels and likelihood information, while doing classification of multispectral remotely sensed images. MRF is used to construct a priori probability function in Bayesian sense so as to estimate the MAP function during the modelling process. For the SR map c, we represent the prior probability function as (c), and the conditional probability function that image y is observed, given the true SR map c as $P(y|c)$. Given the observed image y, the posterior probability function for SR map c is denoted by $P(c|y)$. Since, Gibbs Random Field (GRF) provides a global model for an image, using Hammerley- Clifford theorem (Tso & Mather 2009), the MRF is equivalent to GRF and the above-mentioned probabilities can be formulated by means of energy functions (Geman & Geman 1984).

$$P(c) = \frac{1}{Z_{\mathrm{p}}} \exp(-U(c)/T) \tag{2}$$

$$P(y|c) = \frac{1}{Z_l} \exp(-U(y|c)/T) \tag{3}$$

$$P(c|y) = \frac{1}{Z} \exp(-U(c|y)/T) \tag{4}$$

where Z_{p}, Z_{l} and Z are constants for normalization, T is a constant termed temperature, $U(c)$is a prior energy function, $U(y|c)$ is likelihood energy function and $U(c|y)$ is posterior energy function between true SR map c and observed image y.

Using Bayes' theorem, the relation between the conditional probabilities can be written as:

$$P(c|y)\alpha P(c)P(y|c) \tag{5}$$

For energy functions, the above Equation (5) can be described as:

$$U(c|y) = U(c) + U(y|c) \tag{6}$$

3.4. Prior energy

The prior energy function mentioned in Equation (2) can be described as the sum of pair–site interactions (Li 2009) and formulated as:

$$U(c) = \sum_{i,j} U\big(c(a_{j|i})\big) = \sum_{\mathrm{i,j}} \sum_{l\in \mathrm{N}\left(\mathrm{a}_{j|i}\right)} w(a_l)\cdot \delta\big(c(a_{j|i}), c(a_l)\big) \tag{7}$$

where $U\big(c(a_{j|i})\big)$ is the local contribution to the prior energy from the pixel $c(a_{j|i})$, $w(a_l)$ represents the weight of the contribution from pixel $a_l \in N(a_{j|i})$ to the prior energy, and $\delta(c_1, c_2)$ equals 0, if c_1 and c_2 are same and 1 otherwise. The weight contribution $w(a_l)$ is modelled as:

$$w(a_l) = q\cdot \varphi(a_l) \tag{8}$$

where $\sum_{l\in N(a_{j|i})} \varphi(a_l) = 1$ and $0 \le q < \infty$ controls the overall magnitude of the weights. It provides control on the prior energy term: higher the values of q, smoother the image and vice versa.

3.5. Likelihood energy

It is assumed that the landcover classes are normally distributed and are characterized by mean μ_α and covariance σ_α. Furthermore, assuming the pixels b_i in the observed image y b_i are normally distributed, one can write the statistical parameters mean μ_i and covariance σ_i of the pixels as:

$$\mu_i = \sum_{\alpha=1}^{L} \theta_{\alpha i}\mu_\alpha \tag{9}$$

$$\sigma_i = 1/S^2 \sum_{\alpha=1}^{L} \theta_{\alpha i}\mu_\alpha \tag{10}$$

where $\theta_{\alpha i}$ represents proportion of the class α in the pixel b_i.

The formulation for corresponding likelihood energy can be given as:

$$U(y|c) = \sum_{i,j} U\big(y(b_i)|c(a_{j|i})\big) = \sum_{i,j}\left[\frac{1}{2}(y(b_i)-\mu_i)'\sigma_i^{-1}(y(b_i)-\mu_1) + \frac{1}{2}\ln|\sigma_i|\right] \tag{11}$$

where $U\big(y(b_i)|c(a_{j|i})\big)$ is the local contribution to the likelihood energy from the pixel $c(a_{j|i})$ and σ represents covariance.

3.6. Posterior energy

For the super-resolution map c, the minimum posterior energy is given as:

$$U(c|y) = q \cdot \sum_{i,j} \sum_{l \in N(a_{j|i})} \varphi(a_l) \cdot \delta\big(c(a_{j|i}), c(a_l)\big) + U(y|c) \tag{12}$$

As explained in Tolpekin and Stein (2009), normalization of Equation (12) by a factor $(1+q)$, which is independent of y, results in:

$$U(c|y) \propto \lambda \sum_{i,j} \sum_{l \in N(a_{j|i})} \varphi(a_l)\ \delta\big(c(a_{j|i}), c(a_l)\big) + (1-\lambda) U(y|c) \tag{13}$$

where $\lambda = \frac{q}{(1+q)}, 0 \le \lambda < 1$. The smoothness parameter λ controls the contribution from the prior and likelihood energy in the posterior energy.

By combining Equations (7), (12) and (13), the global energy can be written as:

$$U_{\text{global}} = \lambda U_{\text{priori}} + (1-\lambda) U_{\text{likelihood}} \tag{14}$$

The prediction of pixel value in image x is prepared by minimizing the global energy obtained in Equation (14) and a MAP solution for the SR map c is

$$\hat{\chi} = \arg\min\{\lambda U(c) + (1-\lambda) U(y|c)\} \tag{15}$$

An integrated approach is employed wherein neighbouring pixels has an effect on the estimation of each pixel (Li 2009). In this study, simulated annealing (discussed in Section 3.8) is employed to solve Equation (15) within reasonable time frame. The MRF-based SRM technique, as proposed by Tolpekin and Stein (2009) does not rely on soft classification. In addition to that, the error in the sub-pixel classification result could be corrected in SRM itself. Tolpekin and Stein (2009) did not conduct any experiment to get its result on classification and used equal weights for the likelihood and prior energy constraints.

3.7. Estimation of the smoothness parameter

In MRF-based SRM technique, the smoothness parameter (λ) plays an important role and is estimated beforehand. Generally, λ is determined either by trial and error which can be very time-consuming or using training sites, a computationally expensive procedure. In this research, the internal parameter of MRF-based SRM is firstly estimated by trial and error method and is compared with the optimal smoothness parameter based on a local energy balance analysis as developed in Tolpekin and Stein (2009). To save on processing time for experiments, a subset of ASTER data with a dimension of 12 × 12 pixels was used. Using this subset of the data, an optimal value of λ and its range were estimated at different scale factors ($S = 2$, 3, 4, 5, 6 and 10). Table 1 shows estimated optimal values for λ and its range at each S. Values of λ used in the numerical experiments are 0.1, 0.2, 0.3, 0.4, 0.5, 0.6, 0.7, 0.8, 0.85, 0.9, 0.95 and 0.99. As shown in Figure 3, standard deviation is small for different values of λ; therefore, identification of optimal values of λ was not easy. Another, statistical parameter κ proves to be useful. Mean value of κ is plotted against λ as in Figure 3. The optimal $\hat{\lambda}$ value corresponds to the largest mean κ value (i.e. $\kappa_{\max}$). In addition to that, we choose $\kappa \ge 0.9\ \kappa_{\max}$ as the criterion of closeness to the maximum value to represent the optimal range of λ (Tolpekin & Stein 2009) (Table 1).

Table 1. At different scale factor S, optimal values of λ (underlined) and its range and corresponding κ_{max} with standard deviation are given.

S	λ	κ_{max}
2	0.7–<u>0.9</u>–0.95	0.71 ± 0.02
3	0.7–<u>0.85</u>–0.95	0.70 ± 0.01
4	0.6–<u>0.7</u>–0.99	0.69 ± 0.01
5	0.6–<u>0.8</u>–0.95	0.71 ± 0.02
6	0.5–<u>0.7</u>–0.9	0.69 ± 0.02
10	0.4–<u>0.6</u>–0.8	0.67 ± 0.02

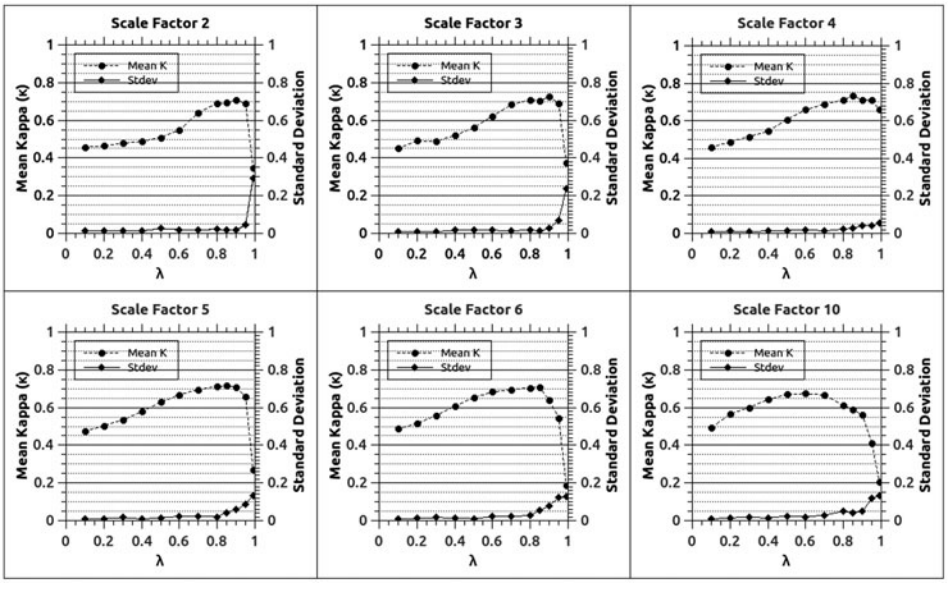

Figure 3. Statistical parameters kappa (κ) and standard deviation are plotted with respect to l different scale factors (S = 2, 3, 4, 5, 6 and 10).

3.8. *Optimization and estimation of* T_0 *and* T_{upd}

Simulated annealing algorithm based on Metropolis–Hastings sampler is applied for optimization of the parameters relating to the minimization of global energy (Geman & Geman 1984). Initial temperature (T_0) and the temperature updating schedule (T_{upd}) are the two parameters of simulated annealing algorithm associated with the magnitude of the posterior energy. The values of the simulated annealing parameters vary according to the scene complexity and are estimated for each image separately. At low temperature, tight coupling between pixels of the image is observed leading to more regular appearance of the image, whereas, at high temperature, the coupling between pixels of image is loosened resulting in noisy image (Geman & Geman 1984). In this research, fine-tuning of the simulated annealing parameters is evaluated on real data set of ASTER image.

Tolpekin and Stein (2009) estimated optimum values of simulated annealing parameter on simulated data for MRF-based SRM and also suggested that one can apply the same optimized values of simulated annealing parameters for different λ values. Geman and Geman (1984), Tolpekin and Stein (2009), and Tso and Mather (2009) suggested that the T_0 values should be set in the range of either 2 or 3. In this research, numerical experiments are conducted to generate the optimal values of T_0 and T_{upd} for ASTER Image. The experiment was conducted for $T_0 = 0$, 1, 2, 3, 4 and 5 for $\lambda = 0.5$ and $S = 3$ and plotted in Figure 4. Three T_0 values (1, 3 and 5) have low mean energy and are close to each other. At the same time, two T_0 values (3, 4) show low standard deviation. Hence, we selected $T_0 = 3$ as an optimum initial temperature parameter T_0.

Simulated annealing parameter T_{upd} optimization was done by varying the values from 0.1 to 0.99 while other parameters (i.e. S and λ) were kept fixed. As shown in Figure 4, it is obvious that from mean κ value, optimal value of T_{upd} could be considered either 0.6 or 0.9. However, considering standard deviation for the two, T_{upd} has minimum. A low standard deviation of κ value indicates that the results are representative for multiple values of parameter value and which is good for reproducibility as well. Hence, $T_{upd} = 0.9$ is considered as optimal temperature updating schedule in this research work.

3.9. *Accuracy assessment*

The accuracy assessment is a critical step in any mapping process and thus is an essential component that allows a degree of confidence to be attached to maps for their effective use.

3.9.1. *Qualitative assessment*

Under this assessment, we have adopted visual interpretation technique which is done manually. Here, interpretation can be done on multiple false colour composites (FCC) of the same remotely sensed image with the help of photo interpretation key elements

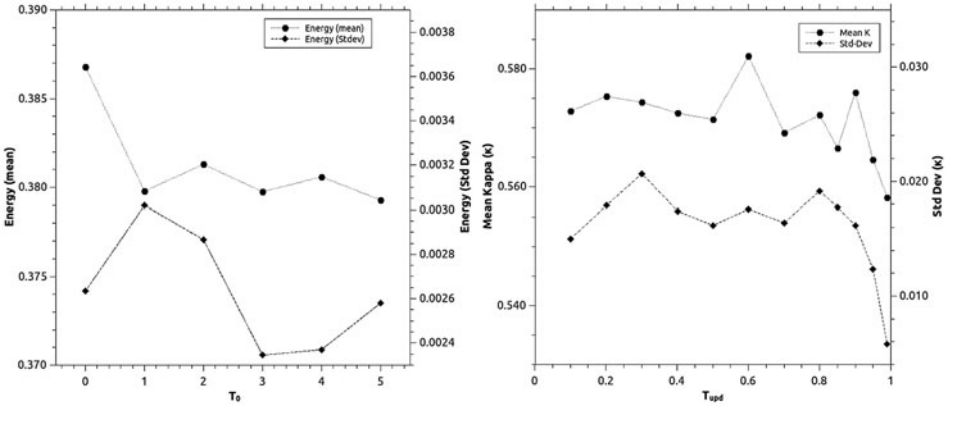

Figure 4. Results from optimization experiments are plotted. Mean energy and standard deviation at varying T_0 are plotted in the left plot. Optimal T_0 is 3. Mean kappa (κ) and standard deviation are plotted for varying T_{upd} in the right plot. Optimal T_{upd} is 0.9.

such as shape, size, tone/colour, texture and association. While on one hand, the technique provides us flexibility of interpretation at desired scale and allows us to apply various enhancement techniques to collect information from the data; on the other hand, it is labour-intensive and is also sensitive to subjective factors.

3.9.2. *Quantitative assessment*

The output classified maps/classes are assessed with the available reference data in terms of user and producer accuracies, overall accuracy and κ values.

3.9.2.1. User accuracy. It is essentially a measure of error of commission. The total number of correct pixels in a category is divided by the total number of pixels that were classified in that category to arrive at user accuracy.

3.9.2.2. Producer accuracy. It refers to the probability that a reference pixel on a map is that particular class itself, indicating how well the reference pixels for that class have been classified. It can be considered as a measure of error of omission.

3.9.2.3. Kappa coefficient (κ). The kappa analysis is a discrete multivariate technique used in accuracy assessment for statistically determining if one error matrix is significantly different from the other (Congalton 1991). Kappa coefficient ranges between 0 and 1.

4. Results

The SRM method based on MRF as described in Tolpekin and Stein (2009) was implemented on an ASTER image to deal with a real-world problem to identify FEs. The study area (Figure 1) is about 5.5 km^2 on the north-western side of the Rutland Island, South Andaman district, ANI, India. The ASTER image of the area has 116 × 334 pixels with 15 m spatial resolution. LISS-IV multispectral remotely sensed data (Figure 5(c)) with spatial resolution of 5.8 m was used to create reference data. The result obtained from MRF-based SRM is compared with MLC. Note that the fraction images were obtained by downscaling of MLC of multispectral image y, which leads to initial model for SRM. Resultant optimized SR map was obtained thereafter. The output of SRM was assessed both qualitatively and quantitatively in comparison with MLC.

4.1. FE identification with ASTER data

Four landcover classes were identified and modelled as FE based on visual interpretation of VNIR bands of ASTER image combined with high-resolution Quickbird data from Google Earth and the LISS-IV standard FCC. These classes are forest, waterbody, degraded forest/land and encroached area. Pure and homogeneous pixels were taken for training sites and the training pixels for these FEs are 344, 2538, 174 and 181, respectively. It was very difficult to find pure pixels for class degraded forest/land and encroached area and is evident in the number of training pixels for these two FEs. The class separability between the classes obtained from transformed divergence method is shown in Table 2.

The reference map was manually digitized from the LISS-IV remotely sensed image which is overlain on all the illustrations from Figures 5–7. While generating the

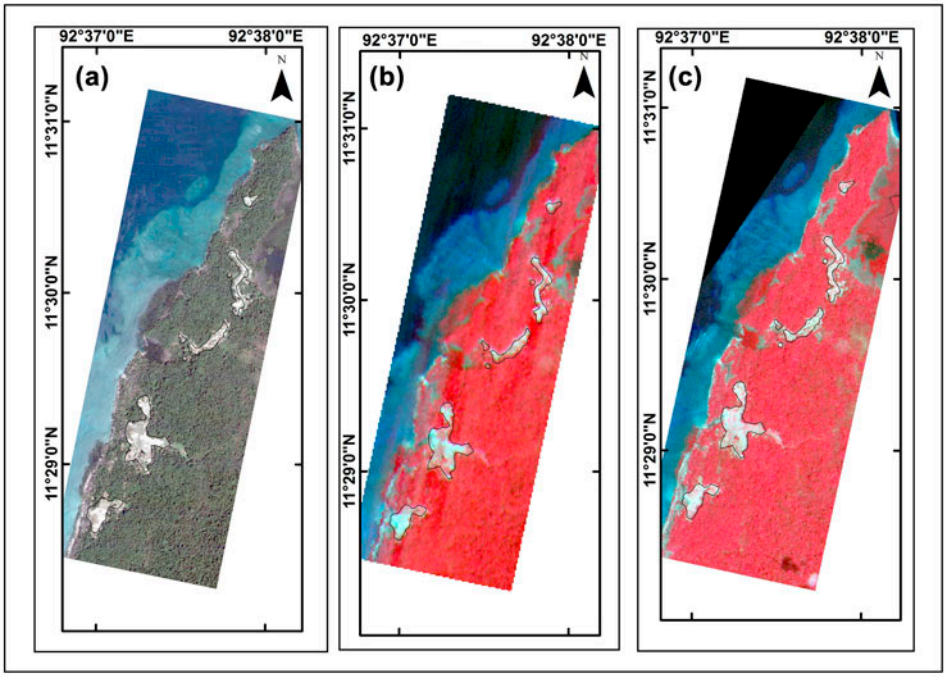

Figure 5. (a) Google Earth data with 0.60 m resolution, (b) ASTER image with resolution at 15 m with band combination of 3, 2, 1 and (c) 3 LISS-IV image with resolution at 5.8 m with band combination of 3, 2, 1.

Table 2. Transformed divergence between the landcover classes at the coarse resolution scale (from the ASTER image).

	Forest	Waterbody	Degraded forest/land	Encroached area
Forest	0	2	2	2
Waterbody	2	0	2	2
Degraded forest/land	2	2	0	1.983
Encroached area	2	2	1.983	0

reference map, visual aid is taken into account using Google Earth data/Quickbird imagery (Figure 5(a)) of the study area with spatial resolution of 60 cm that was acquired on 1 March 2006. The ASTER image (Figure 5(b)), which is used as a test bed, was acquired on 23 February 2006, whereas LISS-IV image (Figure 5(c)), basis of reference map, was acquired on 26 March 2007. Since, there is a difference of thirteen months between reference map data and test bed data, changes in the landcover is expected. In Figure 6, we compare the FEs detected by the SRM with those picked up MLC method. Note that no statistical filter has been applied on these two maps. Clearly, the detected FE pockets are over-smoothed and the result outside of the FE area is noisy. The reference for FE has very sophisticated shapes, for instance Kichad Nallah (as depicted in Figure 7(a)), which cannot be perfectly described by smoothness model

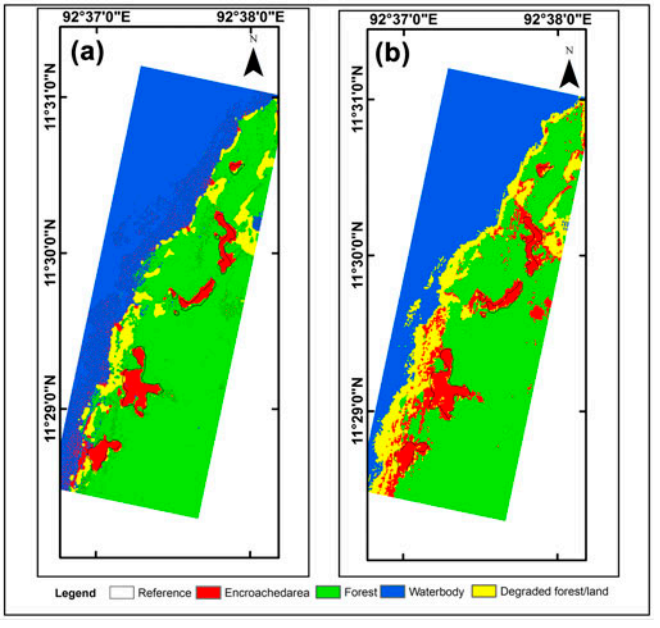

Figure 6. (a) Map showing SRM and (b) MLC map before applying post classification statistical filter.

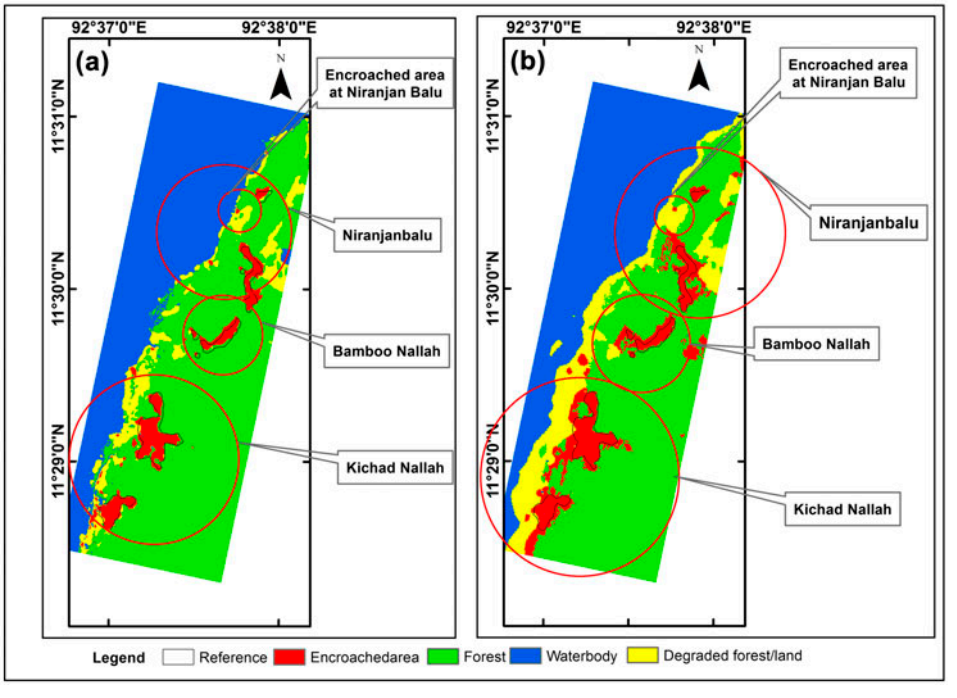

Figure 7. (a) Map showing SRM and (b) MLC map after applying post classification statistical filter with names of FE pockets.

used for SRM. Hence, over-smoothing occurs. In this study, our aim was to detect FE pockets, and as seen, SRM represents them better than MLC.

We further applied statistical filter/majority vote filter using Erdas, 2014 software on the classified maps of SRM and MLC and are shown in Figure 7(a) and (b). From visual interpretation of the two maps with respect to the reference map, clearly, the SRM result is better than the MLC result. Separability of small FE pockets in SRM is better than that in MLC. For example, on the western side of FE locations called Niranjan Balu and Bamboo Nallah. In Table 3, we have compared and listed different features as seen in Figure 7(a) and (b). SRM is consistently performing better in different FE pockets.

We further evaluated the classification results quantitatively. As enumerated in Table 4, MLC method has detected extra area in comparison with SRM method. At Niranjan Balu and Bamboo Nallah, the SRM has detected more than 95% of the target (FE), whereas, at Kichad Nallah, detection of FE is about 93%. Furthermore, small FE pockets at Niranjan Balu have been classified as a big FE pocket in MLC (Figure 7(a)), whereas, small and big FE pockets are detected separately in SRM at the same location (Figure 7(b)). The results are corroborated by field observations. On the basis of the careful qualitative interpretation and quantitative evaluation of the classification results of Figure 7 and as listed in Tables 3 and 4, we can say that SRM outperformed MLC.

4.2. *Accuracy assessment*

In the study area, κ value for MLC is estimated as 0.51, and for SRM, it is 0.62. Accuracy obtained in this study can be improved by using high spectral resolution remotely sensed data, same date of reference and test bed data with spatial resolution equal to output obtained from MRF-based SRM.

According to Tolpekin and Stein (2009), identification of $\hat{\lambda}$ is not very precise in the second decimal place, since estimation was done with step size of 0.1. Therefore, we have further assessed accuracy of the maps with different parameters for λ, T_0 and T_{upd}. In addition to κ, we have also used 'producer's accuracy' and 'user's accuracy' in our assessment and are given in Table 5 for different sets of internal method parameter.

Our optimization process yielded $\hat{\lambda}$, T_0 and T_{upd} as 0.85, 3 and 0.9, respectively. Tolpekin and Stein (2009) obtained $\hat{\lambda}$ as 0.9 and temperature parameters were the same. Statistical measures of accuracy of the maps produced using these two different sets of

Table 3. After running statistical filter, observations inferred from Figure 7(a) and (b).

MLC (see Figure 7(b))	SRM (see Figure 7(a))
On the left hand side between Bamboo Nallah and Kichadnalla, degraded forest/land is mapped in the sea	On the left hand side between Bamboo Nallah and kichadnalla, degraded forest/land is not present in the sea
On the top right hand side of third FE pocket of Niranjanbalu, waterbody is not detected	On the top right hand side of third FE pocket of Niranjanbalu, waterbody is detected
On the easternside on the right hand side of Bamboo Nallah, more than three small patches of false FE is seen	On the easternside on the right hand side of Bamboo Nallah, no FE pocket is visible
In all the detected FE pockets, MLC estimated more area than official record of FE (Table 4)	In all the detected FE pockets, SRM provides areal estimates very close to the values as per official record of FE in the area (Table 4)

Table 4. Quantitative comparison between MLC and SRM classified maps.

Name of FE pockets	Area (Ha)	Area (in Ha) detected by		Difference in area (in %) detected by	
		MLC method	SRM method	MLC method	SRM method
Niranjan Balu	14.4	18	14.2	25 (+)	1.4 (−)
Bamboo Nallah	6	8.6	5.7	43 (+)	5 (−)
KitchadNallah	30.6	38	28.5	24 (+)	7.1 (−)

Table 5. Pixel-based classification errors for FE detection using MLC and SRM for varying optimization parameters.

Tests	Maps	Kappa	User (%)	Producer (%)	Remarks
1	MLC	0.51	38	91	Based on optimized parameters of $\hat{\lambda} = 0.85$, $T_0 = 3$
	SRM	0.59	48	83	and $T_{upd} = 0.9$
2	MLC	0.51	38	91	As per Tolpekin and Stein (2009) $\hat{\lambda} = 0.9$, $T_0 = 3$
	SRM	0.60	49	87	and $T_{upd} = 0.9$
3	MLC	0.51	38	91	Parameters estimated from training sites $\hat{\lambda} = 0.9$,
	SRM	0.62	50	87	$T_0 = 2.8$ and $T_{upd} = 0.89$

parameters are shown in Table 5 (Test #1 and #2). Accuracy measures are in favour of the optimized parameters obtained by Tolpekin and Stein (2009). Therefore, we would expect $\hat{\lambda}$ parameter in the second decimal place to be closer to 0.9 than to 0.85. The effect of small variation in $\hat{\lambda}$ has statistical significance due to the presence of variance of the κ values (Table 1), and it lies in the optimal ranges of λ. According to Geman and Geman (1984), T_0 and T_{upd} varies from simpler to complex case. Therefore, we chose training sites to further optimize T_0 and T_{upd} and are 2.8 and 0.89 giving higher statistical accuracy (Test #3 of Table 5).

5. Discussions

Optimization of simulated annealing parameters is an important step in MRF-based SRM technique. T_0 was fine-tuned by varying its value at a fixed scale factor and λ. Having obtained $T_0 = 3$ as an optimal value, another set of numerical experiments was conducted to obtain the optimal value for T_{upd}. T_0 was kept fixed at 3 while tuning T_{upd} and its optimal value was estimated to be 0.9 for the ASTER image. These two optimal values of simulated annealing parameters were used for all the experiments in this research which in turn provided better results as depicted in Figures 3 and 4. The optimal values of T_0 and T_{upd} were in agreement with the findings of Tolpekin and Stein (2009).

Trial and error method was adopted to find range and optimal value of internal method parameter which is given in Table 1. The statistical parameter κ-based accuracy assessment was used in the decision-making. Optimal range of the internal method parameter is obtained in terms of classification accuracy from κ statistics. The largest mean value of κ (κ_{max}) corresponds to the optimal value of the internal method parameter. Once again, these parameters were in agreement with the findings of Tolpekin and Stein (2009).

For comparison between the object for identification and real ASTER image, scale factor of 3 was chosen which means that our SRM study belongs to H-resolution case (Jupp et al. 1988). Tolpekin and Stein (2009) reported high classification on synthetic images for H-resolution case. Fisher (1997) identified four different types of mixed pixels: boundary, intergrade, small sub-pixels and linear sub-pixel. The mixed pixels which consist of boundaries between two or more mapping units are easier case for SRM. In this research work, we are dealing with mixed pixels of boundary and linear sub-pixel type for FE delineation. The encroached area is modelled as mixed landcover class that contains mainly agricultural land, built-up, grass, bare soil and waterbody. Majority of the encroached area inside the forest of the Rutland Island is being used for cultivation by the encroachers, and it is identified by the visual interpretation of Figure 5(a)–(c) Thus, MRF-based SRM has been effective on real data set dealing with H-resolution.

6. Conclusion

MRF-based SRM method has been effective in detecting FEs. Fine-tuning of simulated annealing parameters is essential for the method to produce desired results. Smoothness parameter was estimated using trial and error method, and findings are in agreement with those reported in Tolpekin and Stein (2009) for normally distributed synthetic data. Since optimal neighbourhood system size varies from one scale factor to another and also computational time increases with system size, it is, therefore, important to prudently choose scale factor and hence window size according the need. The qualities of the SRM were assessed visually as well as quantitatively. The statistics-based κ used as a tool for accuracy assessment indicates that SRM is more accurate than MLC in detecting FE. Different patches of FE are not contiguous; they are spread in various sizes and shapes and are governed by the contextual information. Identification and separability of small and big FE pockets achieved by MRF-based SRM is better than MLC. Although simulated annealing algorithm is computationally expensive for its cooling schedule, speed and parameter estimation, the method produces better results. The results were verified by the headquarter camp officer of the Manglutan range South Andaman forest division, involved in FE identification in the study area.

7. Recommendation and future scope

MRF-based SRM has proved to be an effective tool for detection of FE from ASTER images in Rutland Island, South Andaman, India. On the same line, effectiveness of this method can be explored to detect SLE and tree resources outside forests using other sensors data like LISS-III, LISS-IV and AWiFS. Depending on the availability resources, such studies can be extended to larger areas. Furthermore, simulated annealing algorithm used in this research is computationally expensive; therefore, other optimization methods (e.g. graph cut and belief propagation) can be tested (Tappen & Freeman 2003; Li 2009).

References

Ardila JP, Tolpekin VA, Bijker W, Stein A. 2011. Markov random field based super-resolution mapping for identification of urban trees in VHR images. ISPRS J Photogramm Remote Sens. 66:762–775.

Atkinson PM. 1997. Mapping sub-pixel boundaries from remotely sensed images. Innovation GIS. 4:166–180.

Atkinson PM. 2004. Resolution manipulation and sub-pixel mapping. In: De Jong SM, Van Der Meer FD, editors. Sensing image analysis: including the spatial domain. Netherlands: Springer; p. 51–70.

Atkinson PM. 2009. Issues of uncertainty in super-resolution mapping and their implications for the design of an inter-comparison study. Int J Remote Sens. 30:5293–5308.

Baranga D. 2007. Observations on resource use in Mabira forest reserve, Uganda. Afr J Ecol. 45:2–6.

Boucher A. 2009. Sub-pixel mapping of coarse satellite remote sensing images with stochastic simulations from training images. Math Geosci. 41:265–290.

Boucher A, Kyriakidis PC. 2006. Super-resolution land cover mapping with indicator geostatistics. Remote Sens Environ. 104:264–282.

Bruzzone L, Prieto DF. 2000. Automatic analysis of the difference image for unsupervised change detection. IEEE Trans Geosci Remote Sens. 38:1171–1182.

Congalton RG. 1991. A review of assessing the accuracy of classifications of remotely sensed data. Remote Sens Environ. 37:35–46.

Dijkstra H, Oosterbaan A, van Blitterswijk H. 2003. Kleine landschapselementen. Analyse van de beleidsvraag voor de ontwikkeling van een monitoring systeem [Small Landscape elements: analysis of the policy-making for the development of a monitoring system]. Alterra-rapport, (No. 491). Alterra: Wageningen; p. 70.

Fisher P. 1997. The pixel: a snare and a delusion. Int J Remote Sens. 18:679–685.

Geman S, Geman D. 1984. Stochastic relaxation, Gibbs distributions, and the Bayesian restoration of images. IEEE Trans Pattern Anal Mach Intell. PAMI-6:721–741.

Ghosh A, Subudhi BN, Bruzzone L. 2013. Integration of Gibbs Markov random field and Hopfield-type neural networks for unsupervised change detection in remotely sensed multitemporal images. IEEE Trans Image Process. 22:3087–3096.

Grinand C, Rakotomalala F, Gond V, Vaudry R, Bernoux M, Vieilledent G. 2013. Estimating deforestation in tropical humid and dry forests in Madagascar from 2000 to 2010 using multi-date Landsat satellite images and the random forests classifier. Remote Sens Environ. 139:68–80.

Groom G, Mücher CA, Ihse M, Wrbka T. 2006. Remote sensing in landscape ecology: experiences and perspectives in a European context. Landscape Ecol. 21:391–408.

Jupp DLB, Strahler AH, Woodcock CE. 1988. Autocorrelation and regularization in digital images. I. Basic theory. IEEE Trans Geosci Remote Sens. 26:463–473.

Kasetkasem T, Arora MK, Varshney PK. 2005. Super-resolution land cover mapping using a Markov random field based approach. Remote Sens Environ. 96:302–314.

Kumar GP, Hemanjali AM, Ravikumar P, Somashekar RK, Nagaraja BC. 2013. Assessment of forest encroachment at Belgaum district of Western Ghats of Karnataka using remote sensing and GIS. J Environ Biol. 35:259–264.

Li SZ. 2009. Markov random field modeling in image analysis. London: Springer.

Mehdawi AA, Bin Ahmad B. 2012. Classification of forest change by integration of remote sensing data with neural network techniques. 2012 International Conference on System Engineering and Technology (ICSET); Bandung.

Mertens KC, De Baets B, Verbeke L, De Wulf R. 2006. A sub-pixel mapping algorithm based on sub-pixel/pixel spatial attraction models. Int J Remote Sens. 27:3293–3310.

Mertens KC, Verbeke L, Ducheyne E, De Wulf R. 2003. Using genetic algorithms in sub-pixel mapping. Int J Remote Sens. 24:4241–4247.

Oosterbaan A, Pels M. 2007. Monitoring of small landscape elements in the Netherlands. Landscape Res. 32:95–102.

Sastry KLN, Kandya AK, Thakker PS, Ajai Shangkooptong LB, Devi RS, Singh NS, Singh KJ, Khaizalian, Singh KT, Singsit S. 2007. Nationwide forest encroachment mapping using remote sensing and GIS techniques-Manipur state. Scientific Note: GIDD/GTDG/RESA/SAC/TR-01/DEC 2007. Ahmedabad: Space Application Centre.

Satish KV, Saranya KRL, Reddy CS, Krishna PH, Jha CS, Rao PP. 2014. Geospatial assessment and monitoring of historical forest cover changes (1920–2012) in Nilgiri Bioshere Reserve, Western Ghats, India. Environ Monit Assess. 186:8125–8140.

Sheeren D, Bastin N, Ouin A, Ladet S, Balent G, Lacombe JP. 2009. Discriminating small wooded elements in rural landscape from aerial photography: a hybrid pixel/object-based analysis approach. Int J Remote Sens. 30:4979–4990.

Skaloš J, Engstová B. 2010. Methodology for mapping non-forest wood elements using historic cadastral maps and aerial photographs as a basis for management. J Environ Manage. 91:831–843.

Song DX, Huang C, Sexton JO, Channan S, Feng M, Townshend JR. 2014. Use of Landsat and Corona data for mapping forest cover change from the mid-1960s to 2000s: case studies from the Eastern United States and Central Brazil. ISPRS J Photogramm Remote Sens. 103:81–92. doi:10.1016/j.isprsjprs.2014.09.005.

Stone TA, Brown IF, Woodwell GM. 1991. Estimation, by remote sensing, of deforestation in central Rondônia, Brazil. For Ecol Manage. 38:291–304.

Subudhi BN, Bovolo F, Ghosh A, Bruzzone L. 2014. Spatio-contextual fuzzy clustering with Markov random field model for change detection in remotely sensed images. Opt Laser Technol. 57:284–292.

Tappen MF, Freeman WT. 2003. Comparison of graph cuts with belief propagation for stereo, using identical MRF parameters. Computer Vision, 2003 Conference Proceedings; Nice.

Tatem AJ, Lewis H, Atkinson P, Nixon M. 2001. Super-resolution target identification from remotely sensed images using a Hopfield neural network. IEEE Trans Geosci Remote Sens. 39:781–796.

Tatem AJ, Lewis H, Atkinson P, Nixon M. 2002. Super-resolution land cover pattern prediction using a Hopfield neural network. Remote Sens Environ. 79:1–14.

Thornton MW, Atkinson PM, Holland DA. 2006. Sub-pixel mapping of rural land cover objects from fine spatial resolution satellite sensor imagery using super-resolution pixel-swapping. Int J Remote Sens. 27:473–491.

Tolpekin VA, Ardila Lopez JP, Bijker W. 2010. Super-resolution mapping for extraction of urban tree crown objects from VHR satellite images. ISPRS 2010 Conference Proceedings; Ghent.

Tolpekin VA, Stein A. 2009. Quantification of the effects of land-cover-class spectral separability on the accuracy of Markov-random-field-based superresolution mapping. IEEE Trans Geosci Remote Sens. 47:3283–3297.

Tso B, Mather. 2009. Classification methods for remotely sensed data. New York, (NY): CRC Press, Taylor & Francis Group.

Vega B, Hussin YA, Sharifi A. 2006. Optical and microwave image fusion to detect and monitor illegal logging and tropical rain forest encroachment in east Kalimantan, Indonesia. ACR 2006 Conference Proceedings; October 9–13; Ulanbaatar, Mongolia.

Xu M, Chen H, Varshney PK. 2011. An image fusion approach based on Markov random fields. IEEE Trans Geosci Remote Sens. 49:5116–5127.